EUROFUSION WPS1-PR(15) 14593

R Reimer et al.

On the influence of Zeeman effect on magnetic equilibrium reconstruction using Motional Stark Effect diagnostic

Preprint of Paper to be submitted for publication in
Plasma Physics and Controlled Fusion

This work has been carried out within the framework of the EUROfusion Consortium and has received funding from the Euratom research and training programme 2014-2018 under grant agreement No 633053. The views and opinions expressed herein do not necessarily reflect those of the European Commission.

On the influence of Zeeman effect on magnetic equilibrium reconstruction using Motional Stark Effect diagnostic

René Reimer, Andreas Dinklage, Robert Wolf, W7-X Team
Max Planck Institute for Plasma Physics, 17491 Greifswald, Germany

Oleksandr Marchuk
Institut für Energieforschung-Plasmaphysik, Forschungszentrum Juelich GmbH, Partner in Trilateral Euregio Cluster, 52425 Jülich, Germany

Mike Dunne, Benedikt Geiger, Jörg Hobirk, ASDEX Upgrade Team
Max Planck Institute for Plasma Physics, 85748 Garching, Germany

Patrick J. Mc Carthy
Department of Physics, University College Cork, Association EURATOM-DCU, Cork, Ireland

E-mail: Andreas.Dinklage@ipp.mpg.de / Robert.Wolf@ipp.mpg.de

Abstract.
This work considers the Zeeman Effect (ZE) into the spectral Motional Stark Effect (MSE) diagnostic, a well established technique to infer the local internal magnetic field in fusion plasmas, and studies the influence of the ZE onto the spectrum of the Balmer-α beam emission for different experimental conditions. In order to reveal small (dia)magnetic effects in the magnetic field the accuracy required is quite demanding. With regard to this requirement an existing Forward Model (FM) which fits MSE data to give access to the magnetic quantities is extended by the Zeeman Effect. This extension has an effect of about 1 % in the derived magnetic field strength and of about 1° in the MSE angle compared to the pure MSE case under ASDEX Upgrade conditions. The calculated magnetic field data as well as the revealed (dia)magnetic effects in a high β discharge are consistent with the results from an equilibrium reconstruction solver. The related fast ion pressure variations derived from the spectral Zeeman and Motional Stark Effect (ZMSE) FM data agree within their error range with the fast ion pressure changes calculated by a transport code.

Keywords: Motional Stark Effect, Zeeman Effect, Zeeman-Stark Effect, Beam Emission Spectroscopy, magnetic field measurements, magnetically confined plasmas

1. Introduction

The magnetic configuration of a magnetically confined plasma is strongly related to the local plasma pressure. The magneto-hydrodynamic force balance $\nabla p = \vec{j} \times \vec{B}$ describes a condition for a stationary magnetic equilibria. Changes in the fast ion population can cause diamagnetic effects by increasing the toroidal magnetic field [1, 2]. In order to reveal these small effects of about $\approx 1\,\%$ mainly in the toroidal magnetic field accurate equilibrium reconstruction is essential. To achieve this high accuracy, calculations of equilibrium reconstruction solver based on the solution of the Grad-Shafranov equation are usually constraint by global information from external field measurements and by local information in the plasma.
In this paper spectral MSE measurements of the internal local magnetic field [3, 4] are assessed. The concept relies on the observation of the Balmer-α transition ($n = 2 \rightarrow 3$) from high energetic injected deuterium particles with velocity $\vec{v}_b$ with respect to the background magnetic field $\vec{B}$, excited by collisions on ions and electrons. For practical purposes, the emission is split into 9 observable Stark components by the electric Lorentz field, $\vec{E}_L = \vec{v}_b \times \vec{B}$, acting on atoms in their moving frame of reference. The resulting π ($\Delta m_l = 0$) and σ ($\Delta m_l = \pm 1$) lines of the Stark pattern are polarized parallel and perpendicular, respectively, to the local Lorentz field. Therefore, the polarization of the Stark lines is sensitive to the orientation of the $\vec{E}_L$.
Employing polarization measurements from the central, unshifted $\sigma-$lines allows one MSE angle reconstruction by MSE polarimetry [5, 6, 7]. In spectral MSE measurements the line splitting, $\Delta\lambda$, depends on $|\vec{E}_L|$ and therefore allows to measure $|\vec{B}|$ [8, 9, 3].
The MSE is routinely used as a tool for improved equilibrium reconstruction [10, 11, 12, 13, 14]. However, the desired high accuracies for magnetic field measurement could not be achieved due to a number of inaccuracies in earlier analysis, e.g. correct treatment of the population densities of the upper atomic sub-levels [15, 16, 17]. In addition to that, another atomic physics effect, the Zeeman admixture, was often neglected in the beam emission analysis with regard to the small effect of B compared to the Motional Stark Effect [16]. Combined with the MSE it forms the so-called combined Zeeman-Stark Effect pattern [18, 19, 20, 21].
In this paper, the effect of both strong magnetic and electric fields on the Balmer-α emission is revisited. The atomic physics background is adapted for the application in MSE measurement and the effect on potential admixture due to Zeeman contribution is discussed in view of the spectral MSE measurements. The atomic physics package is prepared for even more refinements which can be done in future, e. g. by including contributions of radial electric fields. A formerly derived beam emission forward model [22] is extended with the combined Zeeman effect on MSE.
In the subsequent chapter the improved model of the MSE measurement is validated on a reference discharge with a variation of the magnetic field. Moreover, variations in the fast ion pressure profiles in a high β discharge scenario are investigated. The results are compared with results from equilibrium solver (CLISTE) [23] and transport code (TRANSP) [24] calculations.

2. Role of electromagnetic fields on emission of moving particles

The influence of the Zeeman Effect (ZE) onto the Balmer-α emission was already identified by Souw et al. [20] and later in the PhD theses by Mandl [25] and Yuh

[16]. Moreover, a rough estimation by the ratio of the most relevant terms of the Schrödinger equation for principle number $n = 3$

$$\frac{\mu_B}{\frac{3}{2}nea_0} \cdot \frac{B}{E_L} = \frac{2\mu_B}{ea_0} \cdot \frac{1}{v \sin\alpha} \tag{1}$$

$$\approx 0.12, \text{ for ASDEX Upgrade} \tag{2}$$

(where μ_B is the Bohr magnetron, a_0 the Bohr radius, v the beam velocity and α the angle between B and v) indicates that the ZE has an measurable effect to the spectrum. Despite these facts the ZE was usually neglected in the analysis of this emission. For the MSEp using the central σ line to determine the MSE angle this simplification is fully justifiable [25, 26]. This is different for the spectral MSE. Here the full spectrum is analyzed to determine both, the MSE angle and the absolute value of B. In this work the effect of adding the ZE to the MSE on the line intensity and the line splitting was determined. Both, the enhancements of the line intensities and of the line splitting allow a more accurate estimation of $|\vec{B}|$ and $\vec{B}$ and can lead to improved equilibrium reconstruction. The following introduction leads to a discussion about the condition when ZE needs to be taken into account.

The geometry used in the present calculation differs to the one used in [16, 20, 25] and is shown in Fig. 1. Contrary to earlier works where the magnetic field points into z-direction, $v_{\perp B}$ lies in the x-y plane and the Lorentz field lies in the x-y plane perpendicular to $v_{\perp B}$ and $\vec{B}$, the coordinate system is chosen to be the y-axis aligned with the magnetic field ($\vec{B} = (0, B_y, 0)$). $\vec{v}$ is depicted to be in the x-y plane ($\vec{v} = (v_x, v_y, 0)$). Thus the component perpendicular to $\vec{B}$ that contributes to the Lorentz field $v_{\perp B}$ points into x ($v_\perp = (v_x, 0, 0)$) and the Lorentz field is parallel to the z-axis, $\vec{E}_L = (0, 0, v_\perp \cdot B_y)$. The direction of observation is represented by $\vec{s}$. The plane normal to $\vec{s}$ is defined by the polarization vectors $\vec{e}_1$ and $\vec{e}_2$. For the general case the presence of additional electric or magnetic fields can be considered, e.g. by including E_r that points perpendicular to $\vec{B}$ and thus lies in the x-z plane ($\vec{E}_r = (E_{rx}, 0, E_{rz})$). This is not explicitly done in the present calculation.

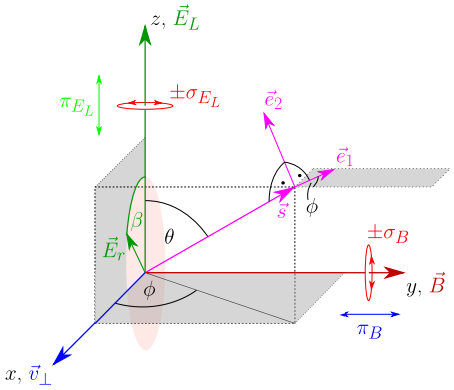

Figure 1. Geometry used in the present calculation (frame of reference and vector orientations): $\vec{B}$..magnetic field, $\vec{E}_L$..Lorentz field, $\vec{v}_\perp$..beam particle velocity, $\vec{s}$..direction of observation, $\vec{e}_1, \vec{e}_2$..polarisation vectors, θ and ϕ..angles determing the observation orientation. The detected emission is polarized in the direction of $\pi_{\mathbf{E_L}}$, $\pm\sigma_{\mathbf{E_L}}$, $\pi_{\mathbf{B}}$, $\pm\sigma_{\mathbf{B}}$ and $\pi_{\mathbf{E_L}}$.

2.1. Effects of electromagnetic fields on Balmer-α

The Balmer-α emission results from the transition of hydrogenic atoms from $n = 3$ (with 18 possible $|i\rangle$ states) to $n = 2$ (with 8 possible $|i\rangle$ states). Here the splitting and the intensity of each transition line is calculated in presence of an electric and a magnetic field oriented as given in Fig. 1. The intensities of the transition lines have a definite spatial characteristic with regard to the polarization and hence depend on the observation angles θ and ϕ. The purpose is to calculate the intensities in plane $\perp$ to the line of sight, $\vec{s}$, with regard to the given basis vectors $\vec{e}_1$ and $\vec{e}_2$. The splitting is determined by the transition energy $\Delta E = E_i - E_j$ for the transition $i \longrightarrow j$ and can be calculated solving the eigenvalue problem

$$\mathbf{H}\psi = E\psi \tag{3}$$

where ψ denotes the hydrogenic wave function and E the eigenvalues. Neglecting the Lamb shift and fine structure, the Hamiltonian $\mathbf{H}$ consists of three contributions

$$\mathbf{H} = \mathbf{H}^0 + \mathbf{H}^{E_L} + \mathbf{H}^B \tag{4}$$

The unperturbed **Bohr** term ($\mathbf{H}^0$) is diagonal in spherical wave functions and is given by

$$H^0_{ij} = \begin{cases} -R_y/n^2, & \text{if i = j} \quad (5a) \\ 0, & \text{if i} \neq \text{j.} \quad (5b) \end{cases}$$

The perturbation caused by Zeeman effect and Motional Stark Effect are represented by the terms $\mathbf{H}^B$ and $\mathbf{H}^{E_L}$, respectively and is calculated in the next sections.

2.1.1. Motional Stark Effect An atom moving with a constant velocity $\vec{v}$ in a magnetic field $\vec{B}$ experiences in its moving frame of reference a Lorentz electric field $\vec{E}_L = \vec{v} \times \vec{B}$.
As shown in Fig. 1, the z-axis is chosen to be parallel to the Lorentz field direction. Thus the Hamiltonian operator for the MSE is given by

$$\mathbf{H}^{E_L} = eBv_\perp z. \tag{6}$$

In order to determine the perturbation caused by the Lorentz field the matrix elements of $\mathbf{H}^{E_L}$ have to be calculated for the z-component: $z^{n,l',m_l'}_{n,l,m_l} = \langle n', m', m_l'|z|n, m, m_l\rangle$, where n is the principal, l the orbital and m_l the magnetic quantum number, here $n' = n$. Writing down the unperturbed wave functions one obtains [27]:

$$z^{n,l',m_l'}_{n,l,m_l} = \int u^*_{n,l',m_l'} z u_{n,l,m_l} d\tau \tag{7}$$

The last integral does not vanish if and only if $m_l = m_l'$. The $z^{n,l',m_l'}_{n,l,m_l}$ are obtained as followed [27]:

$$z^{n,l+1,m_l}_{n,l,m_l} = \sqrt{\frac{(l+1)^2 - m_l^2}{(2l+3)(2l+1)}} R^{n,l+1}_{n,l} \tag{8}$$

$$z^{n,l-1,m_l}_{n,l,m_l} = \sqrt{\frac{l^2 - m_l^2}{(2l+1)(2l-1)}} R^{n,l-1}_{n,l} \tag{9}$$

$$z^{n,l+1,m_l}_{n,l,m_l} = 0, \text{for all other } l' \tag{10}$$

with $R^{n,l-1}_{n,l} = R^{n,l+1}_{n,l} = \frac{3}{2}a_0 n\sqrt{n^2-l^2}$.
Contributions of the radial electric field - which in any case points perpendicular to $\vec{B}$ - is not considered in the present calculation but can be easily considered by substituting $\mathbf{H}^{E_L}$ with $\mathbf{H}^{E} = \mathbf{H}^{E_L} + \mathbf{H}^{E_r}$ and using the β, the angle between E_r and quantization axis:

$$\mathbf{H}^{E_r} = eE_r(-x\sin\beta + z\cos\beta), \tag{11}$$

2.1.2. Zeeman Effect The Zeeman term $\mathbf{H}^B$ is calculated for the strong magnetic field case since the criterion $|\vec{B}| > Z^4$ is fulfilled [28]. The matrix elements are given by

$$H^B_{ij} = \langle n, l', m'_l m' s|\frac{\mu_B}{\hbar}(\mathbf{L} + 2\mathbf{S})\cdot\vec{B}|n, l, m'_l, m'_s\rangle \tag{12}$$

where m_s is the electron spin quantum number and $\mathbf{L}$ and $\mathbf{S}$ denote the orbital and the spin angular momentums respectively. Their scalar products are calculated for each Cartesian component and leads to the following non-vanishing matrix elements [21]:

$$\langle n, l, m_l, m_s|L_x B_x|n, l, m_l \pm 1, m_s\rangle = \frac{\hbar}{2}B_x \cdot \sqrt{(l \pm m_l)(l \mp m_l + 1)} \tag{13a}$$

$$\langle n, l, m_l, m_s|L_y B_y|n, l, m_l \pm 1, m_s\rangle = \pm i\frac{\hbar}{2}B_y \cdot \sqrt{(l \pm m_l)(l \mp m_l + 1)} \tag{13b}$$

$$\langle n, l, m_l, m_s|L_z B_z|n, l, m_l, m_s\rangle = \hbar m_l B_z \tag{13c}$$

and analogue for the spin:

$$\langle n, l, m_l, m_s|S_x B_x|n, l, m_l, m_s \pm 1\rangle = \frac{\hbar}{2}B_x \cdot \sqrt{(\frac{1}{2} \pm m_s)(\frac{1}{2} \mp m_s + 1)} \tag{14a}$$

$$\langle n, l, m_l, m_s|S_y B_y|n, l, m_l, m_s \pm 1\rangle = \pm i\frac{\hbar}{2}B_y \cdot \sqrt{(\frac{1}{2} \pm m_s)(\frac{1}{2} \mp m_s + 1)} \tag{14b}$$

$$\langle n, l, m_l, m_s|S_z B_z|n, l, m_l, m_s\rangle = \hbar m_s B_z \tag{14c}$$

The formulas above are the general case with an arbitrary $\vec{B}$. In this work $\vec{B}$ is directed along the y-axis.

2.1.3. Perturbation The resulting matrix describing the total perturbation from the Lorentz field and the strong magnetic field for $n = 2$ is given in table 1. The matrix operator consists of only non-vanishing off-diagonal matrix elements and shows the following two facts:

(i) The Lorentz field in z-direction leads to an admixture of different l-quantum states

(ii) The magnetic field in y-direction leads to an admixture of quantum states with different magnetic quantum numbers

The abbreviations used in table 1 are lined out below, where the ϕ is the angle between $v_\perp$ and the x axis, which in the present case is 0.

$$\gamma^{(*)} = 3a_0 E_L \tau^{(*)} \tag{15}$$

$$\beta_1^{(*)} = \pm iB \tag{16}$$

$$\beta_2^{(*)} = \frac{\pm i}{\sqrt{2}}B \tag{17}$$

$$\tau^{(*)} = i\cdot\exp(\pm i\phi), \tag{18}$$

		l'=0		l'=1					
	m_l	0	0	1	1	0	0	-1	-1
m_l	m'_s / m_s	1/2	-1/2	1/2	-1/2	1/2	-1/2	1/2	-1/2
0	1/2	0	β_1	0	0	γ^*	0	0	0
0	-1/2	β_1^*	0	0	0	0	γ^*	0	0
1	1/2	0	0	0	β_1	β_2	0	0	0
1	-1/2	0	0	β_1^*	0	0	β_2	0	0
0	1/2	γ	0	β_2^*	0	0	β_1	β_2	0
0	-1/2	0	γ	0	β_2^*	β_1^*	0	0	β_2
-1	1/2	0	0	0	0	β_2^*	0	0	β_1
-1	-1/2	0	0	0	0	0	β_2^*	β_1^*	0

Table 1. Perturbation matrix of $n = 2$ state of a hydrogen atom when experiencing a Lorentz field in z-direction and a magnetic field in y-direction. The abbreviations β_1, β_2 and γ are explained in the abbreviations array 2.1.3.

To obtain the eigenvalues and eigenstates the eigenvalue problem for Eq. 3 must be solved. The matrix operator is hermitian and can thus be diagonalized. The resulting eigenvalues and eigenvectors ψ_i give the level splitting of the multiplet and the corresponding coefficients of the linear expansion in term of the $|n, l, m_l, m_s\rangle$ basis vectors:

$$\psi_i^{(n)} = \sum_{l,m_l,m_s} \langle n, l, m_l, m_s | \psi_i^{(n)} \rangle | n, l, m_l, m_s \rangle \tag{19}$$

Thus the perturbed wave function can be written as a linear combination of the eigenvectors, a_k^i and b_l^j, and the (unperturbed) spherical wave functions, φ_k and φ_l:

- Upper level ($n = 3$): $|i\rangle = \sum_k a_k^i \varphi_k$, with $k = 1 \dots 18$
- Lower level ($n = 2$): $|j\rangle = \sum_l b_l^j \varphi_l$, with $l = 1 \dots 8$

E.g. $|j = 1\rangle = b^1_{|2,0,0,-\frac{1}{2}\rangle} \varphi_{|2,0,0,-\frac{1}{2}\rangle} + b^1_{|2,1,0,\frac{1}{2}\rangle} \varphi_{|2,1,0,\frac{1}{2}\rangle}$ describes the first perturbed state of $n = 2$.

2.1.4. Calculation of line intensities The eigenvalues for the upper and lower level obtained by the calculation described before lead to a repeal of the degenerated lines. As described in the beginning of this chapter the emission characteristics of the polarized transition lines is dependent on the observation angles ϕ and θ, cf. Fig. 1. Hence, in case of a statistical distribution among the sub-levels the intensity of a multiplet component in the directions of $\vec{e}_1$ and $\vec{e}_2$ is

$$I_{(1,2)}^{(ij)} = |\mathbf{D}_{(1,2)}^{(ij)}|^2 \tag{20}$$

with the transition probability

$$\mathbf{D}^{(ij)}_{(1,2)} = \langle i|\vec{e}_{(1,2)} \cdot \mathbf{r}|j\rangle \tag{21}$$

In Eq. 21 the dipole approximation is used to calculate the matrix elements of $\mathbf{D}^{(ij)}_{(1,2)}$ considering their emission characteristic into the direction $\vec{e}_1$ and $\vec{e}_2$. The viewing geometry can be extracted from the left hand side of Fig. 1:

$$\vec{s} = [\sin\theta \cdot \cos\phi, \sin\theta \cdot \sin\phi, \cos\theta] \tag{22}$$
$$\vec{e}_1 = [-\sin\phi, \cos\phi, 0] \tag{23}$$
$$\vec{e}_2 = \vec{s} \times \vec{e}_1 \tag{24}$$
$$= [-\cos\theta\cos\phi, -\cos\theta\sin\phi, \sin\theta] \tag{25}$$

Thus, an expression for the intensity in direction of $\vec{e}_1$ can be given:

$$\mathbf{D}^{(ij)}_1 = \langle i|\vec{e}_1 \cdot \mathbf{r}|j\rangle \tag{26a}$$
$$= -\langle i|x|j\rangle \sin\phi + \langle i|y|j\rangle \cos\phi \tag{26b}$$
$$= -\frac{1}{2}\sum_k \sum_l a^{i*}_k b^j_l \left(\langle k|x|l\rangle \sin\phi + i \cdot \langle k|y|l\rangle \cos\phi\right) \tag{26c}$$

Introducing the $\mathbb{D}$-operator, $\mathbb{D}_\pm = (x \pm iy)$ [20, 27], which describes the semi-axis of the polarization ellipse, gives the possibility to separate linear and circular polarized light. Thus, the last term can be expressed by:

$$\langle k|y|l\rangle = -\frac{i}{2}\left[\langle k|\mathbb{D}_+|l\rangle - \langle k|\mathbb{D}_-|l\rangle\right] \tag{27}$$
$$\langle k|x|l\rangle = \frac{1}{2}\left[\langle k|\mathbb{D}_+|l\rangle + \langle k|\mathbb{D}_-|l\rangle\right] \tag{28}$$

In this case only light polarized perpendicular to the quantization axis (z) can be detected by $\vec{e}_1$. Expressed in the $|n, l, m_l, m_s\rangle$ representation and integration over the angular and radial room leads to [27]:

$$\langle l', m'_l, m'_s|\mathbb{D}_+|l, m_l, m_s\rangle = \delta^{m'_s}_{m_s} \cdot \left[\delta^{l+1}_l \delta^{m_l+1}_{m_l} \sqrt{\frac{(l+m_l+2)(l+m_l+1)}{(2l+3)(2l+1)}} \mathbf{R}^{n',l+1}_{n,l} - \delta^{l-1}_l \delta^{m_l+1}_{m_l} \sqrt{\frac{(l-m_l)(l-m_l-1)}{(2l+1)(2l-1)}} \mathbf{R}^{n',l-1}_{n,l}\right] \tag{29}$$

and

$$\langle l', m'_l, m'_s|\mathbb{D}_-|l, m_l, m_s\rangle = \delta^{m'_s}_{m_s} \cdot \left[-\delta^{l+1}_l \delta^{m_l-1}_{m_l} \sqrt{\frac{(l-m_l+2)(l-m_l+1)}{(2l+3)(2l+1)}} \mathbf{R}^{n',l+1}_{n,l} - \delta^{l-1}_l \delta^{m_l-1}_{m_l} \sqrt{\frac{(l+m_l)(l+m_l-1)}{(2l+1)(2l-1)}} \mathbf{R}^{n',l-1}_{n,l}\right] \tag{30}$$

The radial integrals $\mathbf{R}^{n',l'}_{n,l}$ are given in [27].
The matrix elements in direction of $\vec{e}_2$ can be given analogue:

$$\mathbf{D}^{(ij)}_2 = \langle i|\vec{e}_2\mathbf{r}|j\rangle = -\langle i|x|j\rangle \cos\theta\cos\phi - \langle i|x|j\rangle \cos\theta\sin\phi + \langle i|z|j\rangle \sin\theta \tag{31}$$

with the last term describing the linear polarized component of the MSE multiplet

$$\langle l', m_l', m_s'|z|l, m_l, m_s\rangle = \delta_{m_s}^{m_s'}\delta_{m_l}^{m_l'} \cdot \left[\delta_l^{l+1}\sqrt{\frac{(l+1)^2 - m_l^2)}{(2l+3)(2l+1)}}\mathbf{R}_{n,l}^{n',l+1} + \delta_l^{l-1}\sqrt{\frac{l^2 - m_l^2}{(2l+1)(2l-1)}}\mathbf{R}_{n,l}^{n',l-1}\right] \tag{32}$$

Finally the intensity in direction of $\vec{e}_1$ and $\vec{e}_2$ polarisation can be calculated:

$$I_1^{(ij)} = |\mathbf{D}_1^{(ij)}|^2 \tag{33}$$

$$= |\langle i|x|j\rangle|^2 \sin^2\phi + |\langle i|y|j\rangle|^2 \cos^2\phi \tag{34}$$

$$I_2^{(ij)} = |\mathbf{D}_2^{(ij)}|^2 \tag{35}$$

$$= \underbrace{|\langle i|x|j\rangle|^2 \cos^2\theta\cos^2\phi + |\langle i|y|j\rangle|^2 \cos^2\theta\sin^2\phi}_{\sigma-\text{transition}} + \underbrace{|\langle i|z|j\rangle|^2 \sin^2\theta}_{\pi\text{-transition}} \tag{36}$$

Since $I_2^{(ij)}$ describes either a σ or a π transition one of these terms has to vanish.

2.2. Results: spectral ZMSE line pattern and consequences on physics quantities

2.2.1. Line pattern The model allows one to investigate different cases of physical relevance: the pure ZE case, the pure MSE case and the combination of both, the ZMSE case. Moreover, this approach allows arbitrary directions of $\vec{E}_L$ relative to $\vec{B}$. For the pure ZE case the well known Zeeman line pattern consisting of a central transition line polarized parallel to $\vec{B}$ (π-component) and two lines polarized perpendicular to $\vec{B}$ (σ-component) was observed. The line splitting depends on the magnetic field strength, the line intensity varies with the observation angles ϕ and θ. In the pure MSE case (no $\vec{B}$) with $\vec{E}_L$ pointing into the z-direction the pattern consists of 15 transition lines with an equidistant line splitting, 9 of which are, in practice, detectable. As for the pure ZE case, the individual transition lines are perpendicular polarized (σ) or parallel polarized (π) to $\vec{E}_L$. Summarizing the Einstein coefficients for each polarization state shows that $2\sum_{ij}^{\pi} I^{\pi} = \sum_{ij}^{\sigma} I^{\sigma}$. The relative intensities calculated with this approach agree with [16, 21, 29]. The line splitting depends on the Lorentz field strength and their intensities vary with the observation angles. For observation parallel to $\vec{E}_L$ ($\phi = 0°$, $\theta = 0°$) all components polarized perpendicular to $\vec{E}_L$ are detecable. The observed MSE lines consists of σ-polarized components only. For ASDEX Upgrade relevant discharge parameter ($B = 2.2\,\mathrm{T}$, $E_b = \{10, 15, 30\}\,\mathrm{keV\,/\,amu}$) and geometry ($\phi = 78.61°$ and $\theta = 65.15°$) the line splitting agrees with the one obtained by the MSE-Forward Model, $\mathbf{F}^{E_L}$, [22]. The spectrally resolved multiplet of the combined ZMSE is shown in Fig. 2 (a.). The colors indicate the emission characteristic in the observation direction of $\vec{e}_1$ and $\vec{e}_2$ and the state of polarization: σ-polarized transition lines detected with $\vec{e}_1$ (blue) and detected with $\vec{e}_2$ (red) and π-polarized transition lines which can be observed by $\vec{e}_1$ (green) only. The transition pattern is Doppler-shifted due to the beam velocity and observation geometry and is shown for the aforementioned parameter of the ASDEX Upgrade-MSE. The ZMSE multiplet resembles very much the pure MSE spectrum, three central σ-polarized lines are accompanied by three π-polarized lines each blue

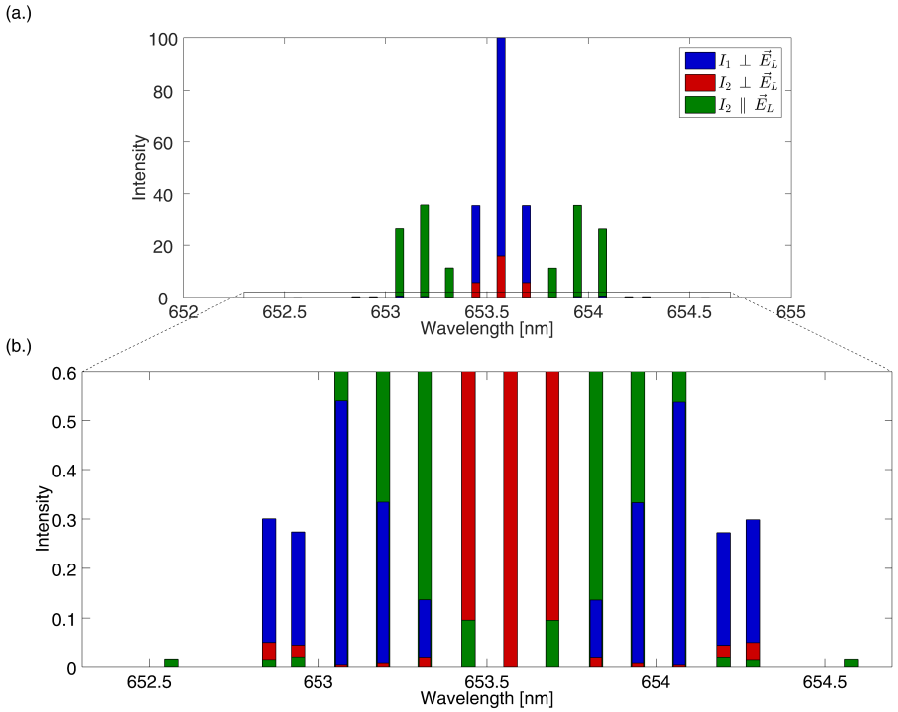

Figure 2. Doppler shifted combined ZMSE spectrum (a.) and a zoom (b.) for full beam energy of ASDEX Upgrade NBI3. The red and blue bars indicate σ-polarized light, whereas the green bars indicate π-polarized light. I_1 and I_2 denote the intensities with respect to the viewing geometry $\vec{e}_1$ and $\vec{e}_2$, respectively.

and red-shifted with respect to the central σ-component. The other 6 lines are almost not detectable. Differently to the pure MSE/ZE cases, the wavelength splitting $\Delta\lambda_{i,j}$ is not equidistant any more and becomes slightly dependent on the specific transition 2 (b.). While this effect is barely expected to affect the MSE data, there is more importantly a mixing effect of different polarization intensities observed. While the mixing of different states gives apparently a minor correction only, it is noted that these spurious contributions may lead to systematic deviations relevant to, e.g., small anticipated effects due to potential fast-ion pressure. The specific impact of the ZMSE effects are addressed in the following chapter.

2.2.2. Impact of Zeeman / Stark mixture effect We now discuss the differences of the MSE and ZMSE model for parameters relevant to the experimental results in the forth-coming sections. For the given experimental conditions Fig. 3 (a.) shows the modelled Doppler-shifted emission pattern for both calculations, MSE and ZMSE, normalized to their maximum value. ASDEX Upgrade relevant beam energies $E_0 = 29.8\,\mathrm{keV}\,/\,\mathrm{amu}$, $E_{1/2} = 14.9\,\mathrm{keV}\,/\,\mathrm{amu}$, $E_{1/3} = 9.95\,\mathrm{keV}\,/\,\mathrm{amu}$ form a pattern represented by the blue, red and green curves. The MSE results are plotted in solid lines the ZMSE results are shown in dashed lines. The ZMSE pattern is plotted in yellow and only slightly deviates from the MSE pattern (black). To reveal the spectral differences between both models the residuum $I_{ZMSE} - I_{MSE}$ is plotted in Fig. 3 (b.). The obtained difference between both models is about $1\,\% - 2\,\%$ of the

maximum intensity. It is noted that the observed mixture effect is strongly related

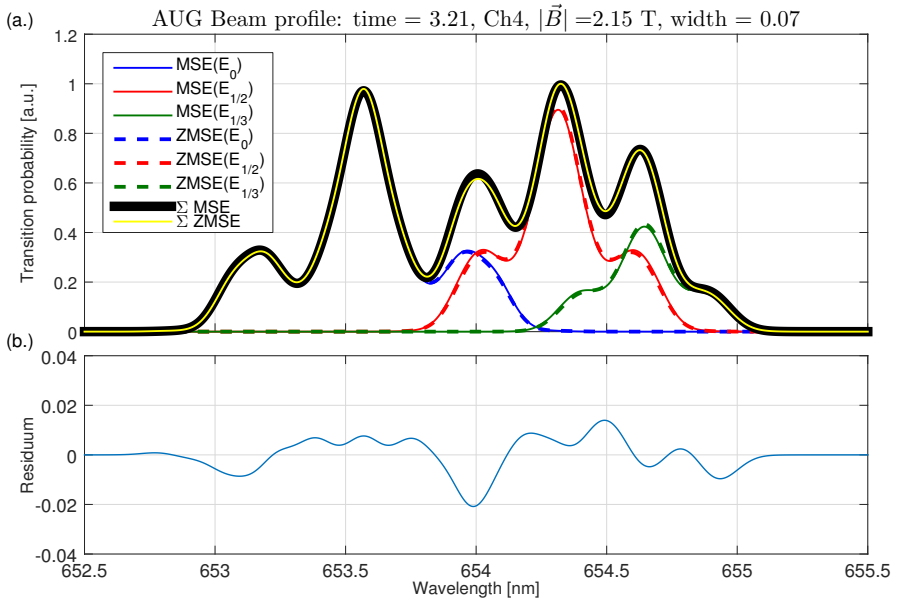

Figure 3. (a.) Doppler shifted beam profile for both MSE (black curve) and MSE-ZE-mix (yellow curve). The MSE (solid lines) and ZMSE (dashed lines) for the individual ASDEX Upgrade beam energies are plotted in blue (full energy component, $E_0 = 29.8\,\mathrm{keV/amu}$), red (half energy component, $E_{1/2} = 14.9\,\mathrm{keV/amu}$) and green (third energy component, $E_{1/3} = 9.95\,\mathrm{keV\,/\,amu}$). A typical ASDEX Upgrade magnetic field of $|\vec{B}| = 2.2\,\mathrm{T}$ was applied. In (b.) the residuum between both, ZMSE- and MSE-spectrum is plotted.

to the chosen geometry setting ($\vec{E}_L$, $\vec{B}$ and $\vec{s}$, cf. Fig. 1). For observation of the emission along $\vec{E}_L$ ($\theta = \pi$, $\phi =$ arbitrary) all polarization directions perpendicular to $\vec{E}_L$ will be observed, (π_B, σ_B and σ_{E_L}). Parallel to $\vec{B}$ ($\theta = \pi$, $\phi = \pi$) all multiplet components which are perpendicularly polarized to $\vec{B}$ are observable (σ_B, σ_{E_L} and π_{E_L}). Thus, besides the polarization mixing, the ZMSE model indicates a slightly different intensity relation $\sum I_\pi / \sum I_\sigma$ compared to the MSE model. The difference is dependent on the geometry, theoretically the relation remains constant.

As discussed above, these findings depend on the observation geometry. In order to discuss the geometry dependence, Fig. 4 (a.) and (b.) show the difference of MSE and ZMSE calculated π and σ-polarized lines in dependence of the orientation of observation. Here the observation angles ϕ and θ are varied from $\phi = [-\pi, \pi]$ and $\theta = [-1/2\pi, 1/2\pi]$. The calculation was done for a beam energy of $E_0 = 30\,\mathrm{keV\,/\,amu}$, the magnetic fields was set to be 2.08 T. For almost all observation angles the admixture of the ZE leads to an increase of the components polarized parallel to $\vec{E}_L$ and, at the same time, a decrease of the components polarized perpendicularly to $\vec{E}_L$. The black box in Fig. 4 indicates the region of ASDEX Upgrade geometry. Here, the effect is about 1.4 % for the parallel component and -0.5 % for the perpendicular component. The changes of the line intensities have impact on the line ratio, T_p, and a correction factor for T_p is introduced as $c_{T_P} = T_{MSE} \,/\, T_{ZMSE}$. For ASDEX beam energies the correction factor is $c_{T_P}(E_0,\, E_{1/2},\, E_{1/3}) \approx \{0.98,\, 0.96,\, 0.94\}$. These

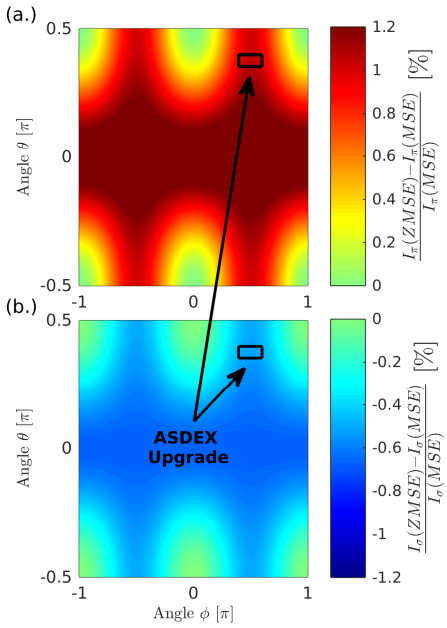

Figure 4. Difference between MSE and ZMSE calculated signal I_π (a.) and I_σ (b.) normalized to its respective MSE calculated maximum in dependence of the geometry. The black boxes show the region of ASDEX Upgrade geometry.

values vary for different channels, due to the different observation angles and magnetic field. The question is, how this affects the physics quantity, γ. The MSE angle is a measure for the direction of the Lorentz field projected in the MSE geometry

$$\gamma = \arctan \frac{E_z}{E_x}. \tag{37}$$

The orientation of $\vec{E}_L$ is determined by the observation angle θ and the direction of the beam. The angle θ is a function of the line ratio

$$\theta = \arccos \sqrt{\frac{1 - T_P}{1 + T_P}}. \tag{38}$$

Fig. 5 shows MSE angles calculated from the spectral MSE (black) and spectral ZMSE data for three ASDEX Upgrade beam energies (blue, red, green) with varying T_P. The thin black lines represent a typical (T_P, γ)-relation as found in the measurements applying the MSE-FM and are used for the discussion below. For the three beam energies the same T_P value leads to the corrected MSE angles indicated by the vertical dashed lines. The effect on the MSE angle measurement is $\Delta\gamma = \{0.44°, 0.88°, 1.32°\}$ is quite significant compared to the required accuracy for fusion devices which is in the range of $0.1° \ldots 0.5°$ [3]. A second finding of the MSE angle analysis is, that the correction increases linear with the applied beam energy but increases slightly non-linear with T_P. It is concluded that MSE angle reconstructions suffer systematically from a neglection of the Zeeman effect and its correction is in the order of about 1 %.

Similar to investigations of Souw et al. [20] and Mandl [21] it was found that for the small beam energy case ($E < 10\,\mathrm{keV}\,/\,\mathrm{amu}$) the line splitting is dominated by the ZE. In this case, the results of both models differ most from each other, e.g. the line

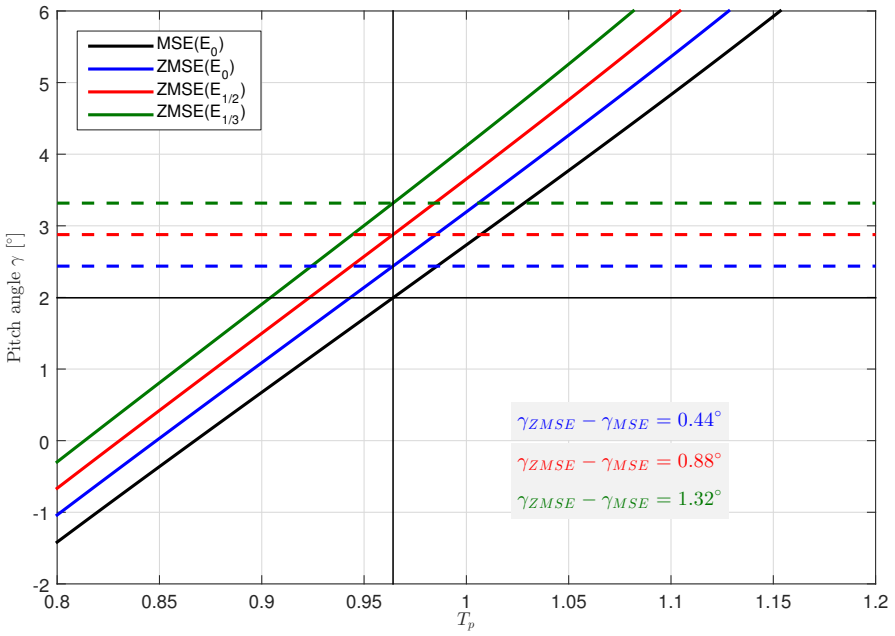

Figure 5. MSE angle variation due to changes in line ratio for three different ASDEX Upgrade beam energies. The thin black lines show a typical (T_P, γ)-relation when applying the spectral MSE-FM. The dashed lines mark the γ value for the same T_P value but calculated with the spectral ZMSE-FM. The colors indicate the certain ASDEX Upgrade beam energy.

splitting between both models can differ by several %. With increasing energy of the injected particles the Doppler-shift and the splitting, dominated by the Stark Effect, increases. For beam energies higher than 30 keV / amu MSE and ZMSE pattern only differ by 1 % in the line splitting. In Fig. 6 the calculated dependence of the physics quantity, $|\vec{B}|$, is shown for varying splitting and ASDEX Upgrade beam energies. The splitting is the mean value taken from most intensive lines ($-4\pi \ldots + 4\pi$). The scattered symbols denote experimental data taken from a magnetic field ramp-down discharge (#26322), the inclined lines represent the fit referred to the experimental data. The color code corresponds to the beam energies. For a magnetic field of about 2.4 T a difference of 1 % (E_0)... 3 % ($E_{1/3}$) can be seen. This is a significant effect and needs to be considered for the calculation of the absolute value of B. However, since the effect depends almost linear on B it can be neglected for interpretation of relative values, for instance in temporal variations of magnetic quantities.

2.3. Improved Forward Model, $\mathbf{F}^{E_L,B}$

The aforementioned formulation of the ZMSE is now included into the forward model that analyses spectral MSE data on ASDEX Upgrade. The forward model to describe the measured data $\vec{d}$ consists of a constant background signal (d_{Bg}), carbon impurity lines ($\vec{d}_{\mathrm{Imp}}$), active charge exchange ($\vec{d}_{\mathrm{CX}}$), a FIDA signal ($\vec{d}_{\mathrm{FIDA}}$) and the ZMSE pattern ($\vec{d}_{\mathrm{ZMSE}}$). Moreover, the cross-talk on the CCD-chip during readout process

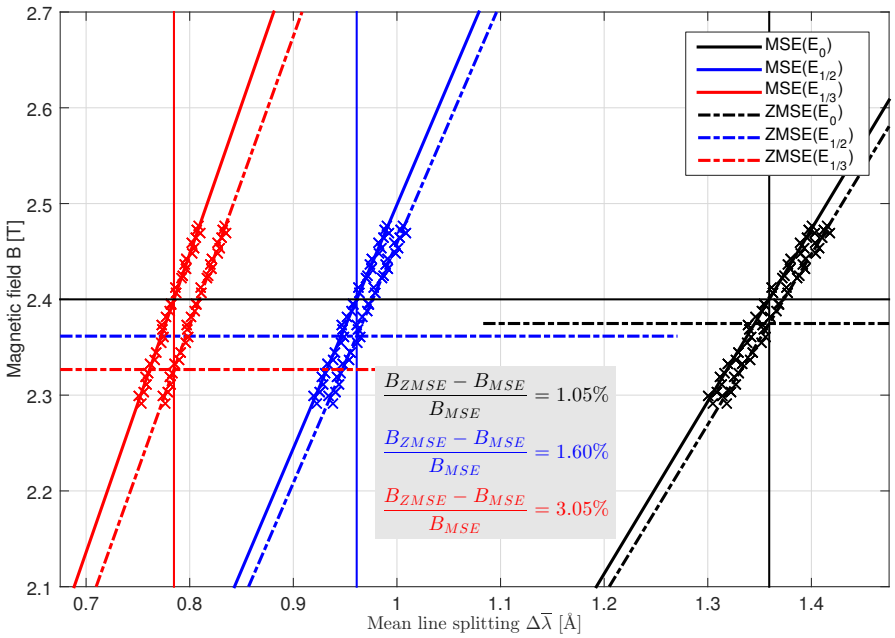

Figure 6. Magnetic field variation as a function of the line splitting at the radial position $R = 1.74\,\mathrm{m}$. The crosses represent MSE (along the solid lines) and ZMSE (along the dashed-dotted lines) calculated splittings corresponding to a magnetic field ramp performed during ASDEX Upgrade discharge 26322. The lines along the experimental data represent a fit to these data. The horizontal black line indicate a magnetic field calculated with CLISTE corresponding to a MSE splitting value (vertical lines). The dashed horizontal lines represent the magnetic field values corresponding to the ZMSE Model evaluated splitting value (vertical lines). The data are represented color-coded for the three beam energies full (black), half (blue) and third (red).

$(\vec{d}_{\mathrm{CT}})$ is included into the FM:

$$\vec{d}(\mathbf{F}^{E_L,B},\vec{p}) = \vec{d}_{\mathrm{ZMSE}} + \vec{d}_{\mathrm{CX}} + d_{\mathrm{Bg}} + \vec{d}_{\mathrm{Imp}} + \vec{d}_{\mathrm{FIDA}} + \vec{d}_{\mathrm{CT}} \quad (39)$$

The parameter $\vec{p}$ reflects all settings, e.g. calibrations. The extension of the forward model in [22] is to include the ZE in the Balmer-α emission. This was done by extending the MSE model from [22] with correction factors for the wavelength splitting and for the intensity relation of the σ and π-polarized Stark lines.
The model of the MSE spectrum considers all 15 (σ and π) Stark components with a spectral profile function constructed by a Gaussian. To consider the different energies, three MSE spectra are modelled using the amplitude, C_{b_i}, the doppler-shifted position of the central σ_0 line, the line position, $\lambda_{E_{L\,i,\pi,\sigma}}$, and the quantity of interest $T_P = \sum I_\pi / \sum I_\sigma$

$$d_{\mathrm{MSE}} = \sum_{i=1}^{3} C_{\mathrm{b}_i} \left(I_\sigma \sum_\pi A_\pi \exp\left[-\frac{1}{2} \left(\frac{\lambda - \lambda_{E_{L\,i,\pi}}}{\sigma_w} \right)^2 \right] + I_\pi \sum_\sigma A_\sigma \exp\left[-\frac{1}{2} \left(\frac{\lambda - \lambda_{E_{L\,i,\sigma}}}{\sigma_w} \right)^2 \right] \right). \quad (40)$$

The Einstein coefficients $A_{\pi,\sigma}$ for the π and σ lines of the Stark spectrum are taken from [29]. The width σ_w is mainly affected by the beam width and the instrument function. For the wavelength mapping a quadratic dispersion relation was determined by three natural neon lines ($\lambda_{\mathrm{Ne1}} = 650.65\,\mathrm{nm}$, $\lambda_{\mathrm{Ne2}} = 653.26\,\mathrm{nm}$, $\lambda_{\mathrm{Ne3}} = 659.87\,\mathrm{nm}$). Additionally, a channel dependent shift of the wavelength scale ($\Delta\lambda_0$) due to imperfections of the optics was added [30].
Non-statistical distribution of sub-levels are considered by a density, megnetic field and beam energy dependent parameter, c_{ns}, that was calculated by a collisional-radiative model [15] and used as a correction factor for T_P

$$T_P^{ns} = c_{ns} \cdot T_P. \tag{41}$$

It need to be noted that factor c_{ns} is in the range of 0.8 ± 0.04, which implies an angle correction of about $\Delta\gamma_{ns} \approx 3°$.
In order to take into account changes in the line ratio and the line mixing effect in the ZMSE case shown in Fig. 2 and Fig. 4, a correction for the line ratio T_P has to be done analogue to the statistical plasma correction in Eq. 41. Thus, the corrected line ratio is

$$T_P^{ns,ZMSE} = c_{T_P} \cdot T_P^{ns}. \tag{42}$$

To consider the line splitting of the ZMSE pattern in the Forward Model the calculated splitting difference between MSE- and ZMSE-model is implemented line dependent in the Forward Model

$$\lambda_{(E_L,B)_{i,\pi,\sigma}} = \lambda_{E_{L\,i,\pi,\sigma}} + \Delta\lambda_{(E_L,B)_{i,\pi,\sigma}}. \tag{43}$$

Thus the full description of the ZMSE pattern in the forward model is:

$$\begin{aligned} d_{\mathrm{ZMSE}} = \sum_{i=1}^{3} C_{\mathrm{b}_i} \Bigg(& I_\sigma \sum_\pi A_\pi \exp\left[-\frac{1}{2} \left(\frac{\lambda - (\lambda_{E_{L\,i,\pi}} + \Delta\lambda_{(E_L,B)_{i,\pi,\sigma}})}{\sigma_w} \right)^2 \right] \\ & + I_\pi \sum_\sigma A_\sigma \exp\left[-\frac{1}{2} \left(\frac{\lambda - (\lambda_{E_{L\,i,\sigma}} + \Delta\lambda_{(E_L,B)_{i,\pi,\sigma}})}{\sigma_w} \right)^2 \right] \Bigg). \end{aligned} \tag{44}$$

3. Validation of the improved Forward Model based on a magnetic ramp-down reference discharge

3.1. Reference discharge

In order to validate the forward model, a reference discharge has been conducted on ASDEX Upgrade. The discharge parameter were chosen to reflect conditions which have been analysed with the CLISTE equilibrium code [31, 23]. Fig. 7 shows the time evolution of the discharge indicating a stationary plasma current of $I_p = 0.8\,\mathrm{MA}$ (a.) and a stationary heating of $P = 5.8\,\mathrm{MW}$ (b.) but a decrease of the toroidal magnetic field from $B_{tor} = -2.6\,\mathrm{T}$ to $B_{tor} = -2.4\,\mathrm{T}$ (a.). B_{tor} has been decreased by lowering the toroidal field coil current.
Fig. 8 shows the temporal evolution of the Lorentz field $\vec{E}_L = \vec{v} \times \vec{B}$ from both an independent analysis of CLISTE (blue) and from the fitted data of the previously discussed forward model (red). The panels represent different locations as indicated by their respective R and z values. The CLISTE data are directly derived from $\vec{E}_L^{CL} = \vec{v}_\perp \times \vec{B}^{CL}$, where $\vec{v}_\perp$ is taken from calibration measurements of the Beam and MSE geometry and $\vec{B}^{CL}$ is a result of the solution of the Grad-Shafranov-Equation [32] in CLISTE. The forward modelled Lorentz fields are calculated with the

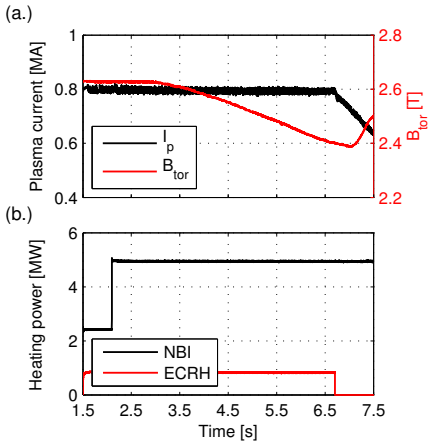

Figure 7. Reference discharge on ASDEX Upgrade (#26322): (a.) Time traces of the toroidal magnetic field (red) and the plasma current (black); (b.) applied plasma heating consisting of NBI (black) and ECRH (red) heating power.

Schwartzschild-Epstein equation [29]. The CLISTE calculations were constrained by magnetic measurements, q and the total pressure ($p_{tot} = p_{kin} + p_{FI}$). Since sawtooth activity has been observed, the safety factor was set $q = 1$ at the axis. In fact this is not exact but setting $q = 1$ at the inversion radius ($\rho_p pprox 0.23$) lead to almost the same results. The kinetic contribution of the total pressure, $p_{kin} = k_B \cdot (n_e T_e + n_i T_i)$, was obtained from kinetic measurements and integrated data analysis (IDA) [33]. The fast ion pressure contribution, p_{FI}, was calculated with the transport code TRANSP [24].

The linear ramp down phase between $t = 3.8\,\mathrm{s}$ and $t = 6.2\,\mathrm{s}$ was assumed to follow the linear decrease of B_t and fitted by a linear model. The precision for each channel was estimated from the sum of the squared residuals. The resulting 2σ error intervals are represented by the shaded regions and are about the same order for CLISTE and FM data. However, in contrast to the CLISTE data the precision of the FM data was found to be channel dependent. With $\sigma = 0.2\,\%$ the error is the lowest at the outermost channel and rises towards the plasma core with a maximum value of $\sigma = 1.5\,\%$ for the innermost channel. This can be explained by the beam attenuation which leads to a decreasing signal-to-noise level towards the plasma.

The results show a small radius dependent difference in the bias and a good agreement for the temporal variation between both methods. In order to analyse the agreement in more detail both fit factors, the bias, E_{L0}, and the inclination, m, are shown in Fig. 9 (a.) and (b.) with there uncertainty. The bold black lines represent the values from the fitted CLISTE data and the dashed black lines represent the values from the fit of the sZMSE data. The blue curves, which are related to the right y-axis, show the normalized difference between both methods in the fit parameter. The normalization factor in (a.) is the the mean value for the bias, $\overline{E}_{L0} = (E_{L0}(CL) + E_{L0}(\mathbf{F}^{E_L,B}))/2$. Δm was normalized by the mean value for the inclination, $\overline{m} = (m(CL) + m(\mathbf{F}^{E_L,B}))/2$, cf. (b.).

It can be seen in (a.) that in for the three locations $R = \{2.0\,\mathrm{m}, 1.90\,\mathrm{m}, 1.74\,\mathrm{m}\}$ the deviation in the bias differs within the range of $0.8\,\%$, for the other three locations

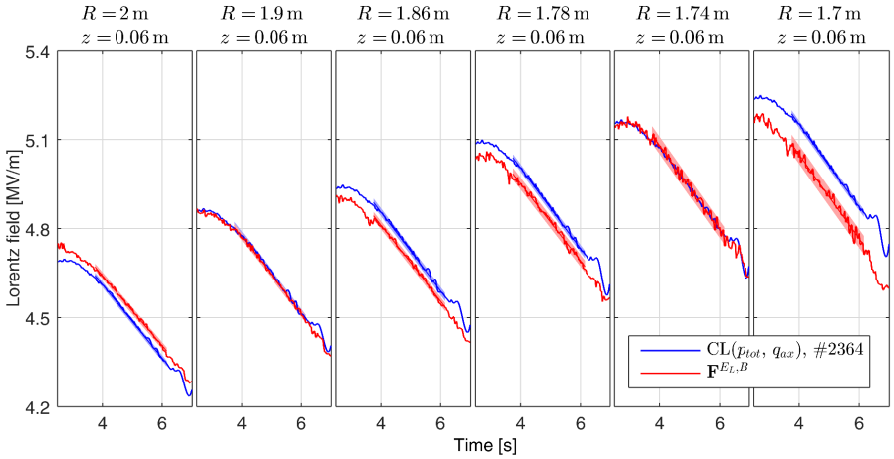

Figure 8. Discharge #26322: Time traces of the Lorentz field calculated with the CLISTE equilibrium code with run# 2364 (blue) and with the ZMSE forward model (red): For both methods the fit functions (straight lines) and the related *rmse* confidence intervals (shadowed regions) are given.

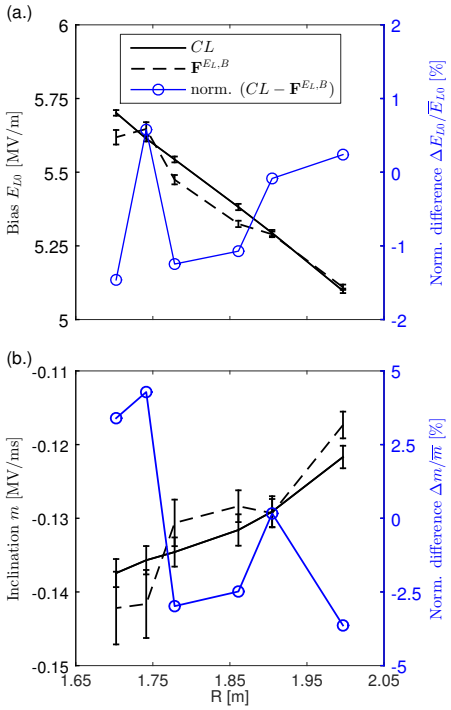

Figure 9. Fit parameter of the linear fit of the magnetic field variation in discharge #26322: (a.) Bias, E_{L0}, (b.) inclination, m, for values of the CLISTE fit (black solid) and of the sZMSE fit (black, dashed). In blue the differences of both methods in the fit parameter are shown normalized by their mean ($\Delta E_{L0}/\overline{E}_{L0}$ and $\Delta m/\overline{m}$), respectively.

the difference is between 1.0 %...1.5 % which is beyond the error range of the certain channel. The reasons for the channel dependent systematic error could be:

(i) Imperfections in the optics components in the sMSE set-up: e.g. by non-optimal adjustment of the detection components which consists of a spectrometer, an objectives and a CCD-chip. The sMSE diagnostic is described in detail in [22]

(ii) Use of a improper profile function for the MSE lines: in the present work a gaussian profile was applied. However, this is not exact. Dux has shown in [34] that the MSE profile is asymmetric due to the variation of the magnetic field along the line-of-sight when it is crossing a beam with a certain width. The effect is the strongest in the innermost channel.

In contrast to the bias the inclination, shown in (b.), is not affected by the systematic errors. The small maximal deviation of about ±4 % for the applied linear decrease of approximately 6 % in the magnetic field lead to a total error in the variation of the Lorentz field of $\Delta m/\overline{E}_{L0} \approx 0.2\,\%$.
It can be concluded that with the given precision and accuracy local variations in the magnetic fields of less 0.05 % can be detected. Moreover, except for the innermost channel at $R = 1.70\,\mathrm{m}$, the sZMSE diagnostic can be used for the measurement of absolute values of the local magnetics with a high accuracy of about 1 % or even better. To improve the consistency with CLISTE results in the measurement of the absolute values the difference in the bias has to be minimized. This could be done by applying asymmetric MSE profile functions and by increasing the accuracy. However, the findings show that the application of the ZMSE FM is a suitable tool to confirm and, moreover, to improve equilibrium reconstructions.

4. Fast ion effects in NBI heated high β discharge

4.1. Discharge overview

In order to asses the potential sensitivity of spectral MSE measurements to fast-ion effects a discharge with stepwise increasing heating power up to 10.8 MW was investigated. Purpose of the experiment was to examine the effect on the plasma equilibrium. Fig. 10 shows relevant time traces of discharge# 26323 on ASDEX Upgrade. Fig. 10 (a.) indicates the applied heating: Electron cyclotron heating (ECRH) was applied in order to prevent tungsten accumulation in the plasma center [35, 36, 37]. Neutral beam injection (NBI) heating with deuterium beams was provided by four 2.5 MW NBI sources for $t > 1.2\,\mathrm{s}$. The more tangentially off-axis deposited heating power of the injected NBI6, the more radially on-axis heating power of NBI8 and NBI5 are added to beam heating of NBI3 used for the sMSE diagnostic. Details about the geometry of the applied beams can be seen in Fig. 11 which shows the toroidal (a.) and poloidal view (b.) of ASDEX Upgrade. Fig. 10 (b.) indicates the total toroidal plasma current with $I_p = 0.8\,\mathrm{MA}$ during the flat-top phase ($t > 0.8\,\mathrm{s}$) and the external toroidal magnetic field of $B_{tor} = -2.48\,\mathrm{T}$. Fig. 10 (c.) and (d.) show the temperature and density: the black lines represent the central electron temperature (T_e) and central electron density (n_e) determined by the integrated data analysis diagnostic (IDA). The red lines indicate the central ion temperature measurements (T_i) from charge exchange recombination spectroscopy and the central ion density (n_i) resulting from n_e and Z_{eff} [38, 39]. The latter has a value of about $Z_{eff} \approx 1.5$. The periodic oscillations in the kinetic signals, especially in the ion and

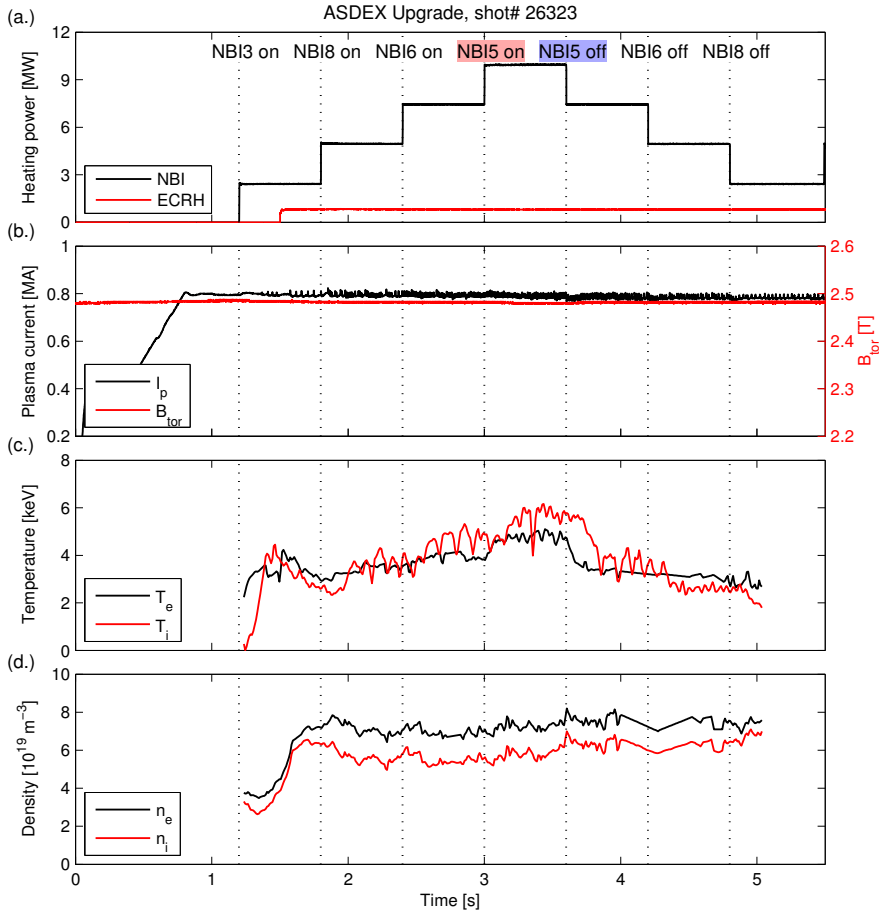

Figure 10. Time traces of important discharge parameters and quantities of discharge 26323 on ASDEX Upgrade: heating power (a.), plamsa current and toroidal magnetic field at axis (b.), temperature (c.) and density (d.) of ions and electrons.

electron temperature time traces reflect the occurrence of sawtooth activity in the plasma. The main aspects are the stepwise increase and decrease of the NBI heating power at time points indicated by the vertical dotted lines. The fact that the NBI sources differ in the direction of injection (Fig. 11 and [22]) is of high importance when discussing equilibrium results.

4.2. Fast ion pressure variation deduced from the forward modelled Lorentz field variation

In this section the variation of both, total and fast ion pressure are derived from the Lorentz field as an application of the spectral combined Zeeman-Stark effect diagnostic. The results are compared to results of the equilibrium solver CLISTE and the transport code TRANSP.
In Fig. 12 (b.) the time traces of the kinetic pressure, derived from the given

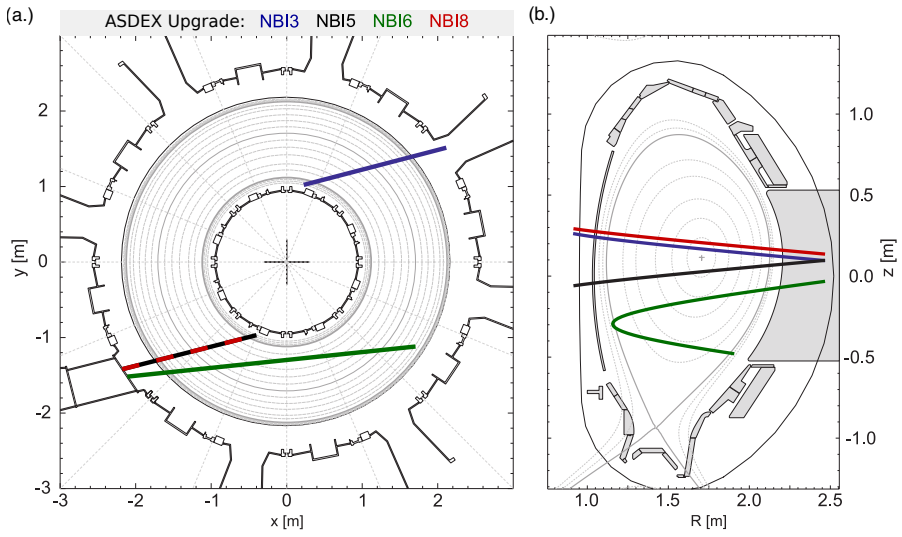

Figure 11. Geometry of applied neutral beam injection for discharge# 26323 - toroidal (a.) and poloidal (b.) view. Since NBI5 and NBI6 are injected from the same NBI box with the same toroidal orientation they are shown in dashed lines in the (a.).

experimental data $p_{kin} = k_B \cdot (n_e T_e + n_i T_i)$, the fast ion pressure, p_{FI}, gained from the transport code TRANSP and the magneto-hydrodynamic pressure, $p_{mhd} = p_{kin} + p_{FI}$, are presented. Furthermore, the stored fast ion and magneto-hydrodynamic energies, calculated with TRANSP are given in (b.). The according time evolutions of the Lorentz fields and MSE angles calculated with the MSE FM, $\mathbf{F}^{E_L}$ and the improved forward model $\mathbf{F}^{E_L,B}$ are shown in (c.) and (d.) for a central channel.
The NBI heating sources mainly generate fast ions into the direction of heating. Since NBI3, NBI5 and NBI8 point more perpendicular and only NBI8 more parallel to the magnetic field there is a higher production of fast ions with perpendicular velocity. Hence, the fast ion pressure is anisotrop. The TRANSP results confirm this and show a relation for the fast ion pressure of $p_{FI,\perp}/p_{FI,\parallel} \approx 1.3$. However, the applied equilibrium solver CLISTE does not take into account pressure anisotropy. Thus the fast ion pressure is assumed to be isotrop for the forthcoming analysis.
The time traces of the central total pressure and central total energy reflect the heating pattern: additional NBI heating leads to a rise and reduced NBI heating leads to a decrease of these quantities. The diamagnetic decrease in the magnetic field due to the rise in the total pressure can be observed in the decrease of the modelled Lorentz field in (c.). This effect is reduced for lower total pressures. This behaviour is mainly related to changes in the toroidal magnetic field whereas variations in the MSE angle, shown in (d.), are mainly related to changes in the poloidal field. According to the findings in Sec. 2.2.2 the Zeeman Effect does not significantly change the shape of the Lorentz field and the MSE angle but contributes as an offset in these magnetic quantities. As can be seen in Fig. 12 (b.) additional NBI heating not only increases the thermal plasma pressure but also increases the production of high energetic particles (fast ions). The high contribution of the fast ion pressure in the total pressure of more than 30 % indicates that the generated fast ions lead to detectable changes in

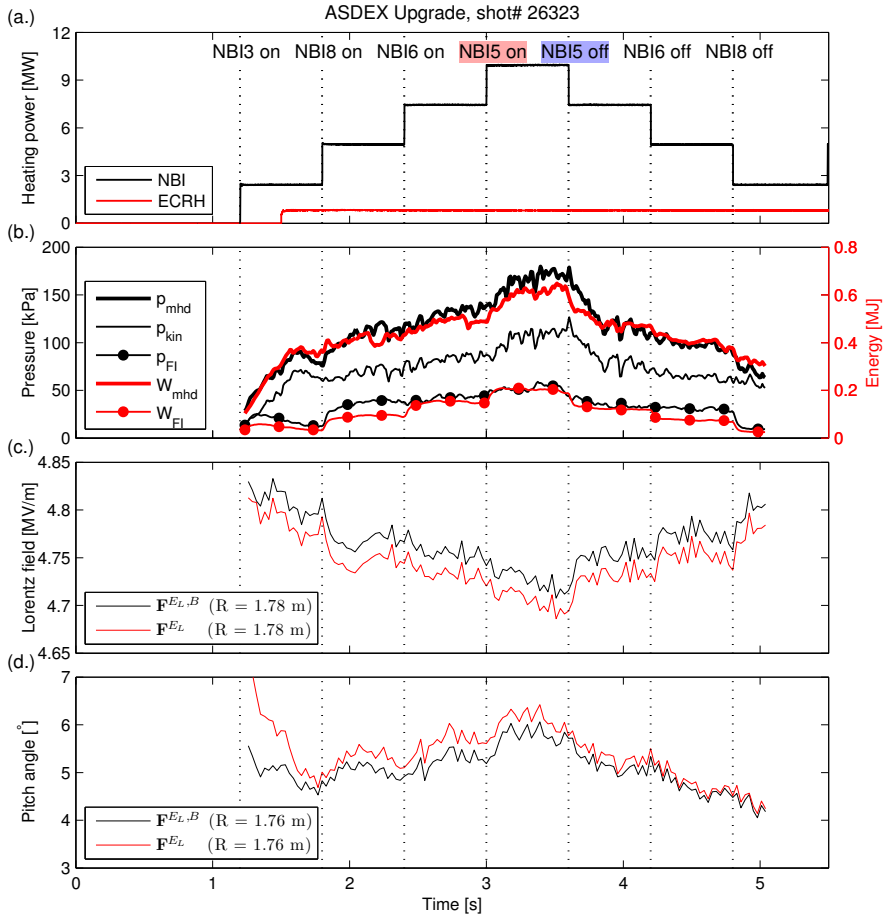

Figure 12. Time traces of central kinetic, mhd and fast ion pressure as well as the related stored mhd and fast ion energies (b.). The time evolution of the forward modelled Lorentz fields and MSE angles are shown in (c.) and (d.), respectively.

the magnetic configuration and need to be considered in equilibrium reconstruction. In Fig. 13 the time evolution of the Lorentz field calculated with the improved forward model (a.) is compared to results of CLISTE (b.) for five different radial positions. On top of the figures the applied method is labelled. As in sec. 3.1 the CLISTE run was constrained by magnetic measurements by the pick-up-coils outside the plasma, the safety factor on the magnetic axis ($q_{ax} = 1$) and by the total pressure profile.
The time traces of CLISTE calculated signals show a significant response on the heating variation consistent to the findings for the forward modelled Lorentz fields in Fig. 12 (c.). The stepwise increase and decrease of the NBI heating power lead to a change in the measured Lorentz field followed by an exponential decay phase. As similar to findings discussed in the previous section, the $\mathbf{F}^{E_L,B}$ data show a lower noise level for the outer channels than CLISTE data. In contrast to the CLISTE data the noise rises towards the plasma core due to the beam attenuation. In order to calculate the Lorentz field variation due to changes in the heating scenario the CLISTE and Forward Model data were fitted with a simple mathematical model that describes the

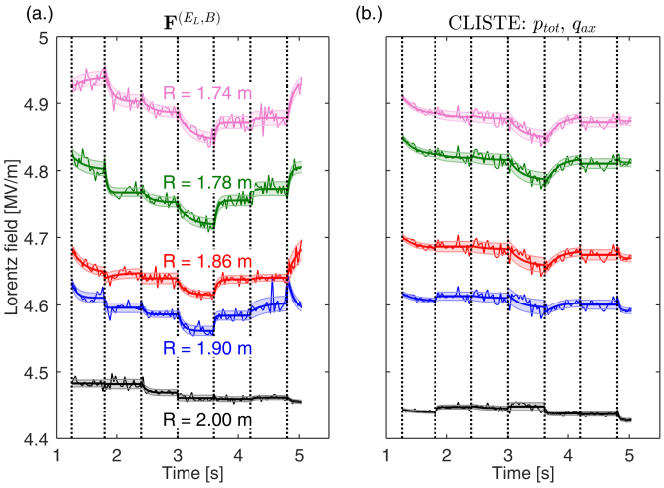

Figure 13. Lorentz field calculated with ZMSE Forward model (a.) and CLISTE right (b.). The CLISTE run was constrained by magnetic edge data and by a total pressure profile, q was set 1 at the axis. The data were fit with an exponential approach as shown by Eq. 45. The shadowed regions indicate the 1σ *rmse* error band of the fit.

exponential decay in the data:

$$E(t) = E_0 + \Delta E \left(1 - \exp\left(-\frac{t_0 - t}{\tau_D}\right)\right), \tag{45}$$

with the fit parameter E_0 denoting the Lorentz field at the beginning of each heating phase, ΔE denoting the amplitude of the change of the Lorentz field and τ_D the decay time. The latter fit parameter is a measure for the confinement times in ASDEX Upgrade. The obtained values differ in a range of 20 ms . . . 160 ms with a high uncertainty of about 50 ms due to the high noise and low time resolution in the data. However, these times agree in magnitude with the knowing slowing down times of fast ions and with the energy confinement time for the ASDEX Upgrade, which are about 60 ms. t_0 and represents the onset-time of each heating scenario phase. All four parameter are dependent of the heating interval and of the position (R, z). The shaded area indicates the 1σ interval of confidence of the fit. The channel dependent deviation of 0.45 % (Ch1). . . 1 % (Ch4) with a mean deviation of $\overline{rms} = 0.7\,\%$ indicates a good agreement between these models for this discharge. Both models show a similar response on the heating variation in the calculated Lorentz field. From the related Lorentz field variation the total pressure variation can be deduced using the pressure balance equation in cylindrical approximation

$$\frac{dp}{dr} + \frac{B_{pol}}{\mu_0 r} \cdot \frac{d\,(rB_{pol})}{dr} = j_{pol} B_{tor}, \tag{46}$$

with the poloidal current density

$$j_{pol} = -\frac{1}{\mu_0} \cdot \frac{dB_{tor}}{dr} \tag{47}$$

the magnetic permeability μ_0 and the minor radius r. For the diamagnetic limit, where the pressure gradient is the dominating part Eq. 46 can be reduced to

$$\frac{d}{dr}\left(p + \frac{B_{tor}^2}{2\mu_0}\right) = 0 \tag{48}$$

Considering the fact that the Lorentz field variation is about the toroidal field variation the pressure balance equation for the diamagnetic limit can be written as:

$$\Delta p \approx -\frac{\Delta E_L^{Dia}}{E_L} \cdot \frac{B^2}{\mu_0}, \tag{49}$$

In order to take into account the diamagnetic effect only ΔE_L^{Dia}, Lorentz field changes due to the Shafranov shift, ΔE_L^S, need to be subtracted from the measured total variation of the Lorentz field ΔE_L^m. The contribution of the Shafranov shift to the total field variation is calculated by the CLISTE equilibrium code and is about $\Delta E_L^s / \Delta E_L^m \leq 10\,\%$.

In Fig. 14 (a.) and (b.) the profiles of the pressure variations for the most significant cases (when NBI5 is switched on (a.) and off (b.)) are presented. Results from different methods TRANSP (mhd), kinetic measurements (kin), Forward Model ($\mathbf{F}^{F_L,B}$) and CLISTE (CL) are compared with each other. Consistent to the findings in Fig. 12 (b.) additional heat load leads to a rise and reduced heating to a decrease of the total pressure and kinetic pressure. The effect of the heating is most significant in the plasma center, here $|\Delta p_{tot}| \approx 40\,\text{kPa}$ and $|\Delta p_{kin}| \approx 23\,\text{kPa}$ when NBI5 is switched on. Towards the the plasma edge the pressure variation vanishes. This indicates that the pressure profile gradient increases with additional NBI heating and vice versa. These findings were also reflected by the Forward model data. In fact, within their range of error, the forward modelled data (black bold line) show a good agreement with the total pressure results from TRANSP (black dashed line) for both, NBI5 on and NBI5 off, cases. Moreover, these results are consistent with the determination of the total pressure variation by CLISTE. It should be noted that the CLISTE calculations showed low sensitivity to the pressure profile it was constrained with, which indicates that CLISTE is operating at its limit of sensitivity. In the error the channel and time dependent uncertainties of ΔE_L, E_L and of B are included.

With the knowledge of the kinetic pressure change the fast ion pressure variation can be calculated. The results (black line with symbols) are compared with the TRANSP calculations (red dashed lines) in the panels (c.) and (d.) of Fig. 14 for the transitions NBI5 on and NBI5 off. Although there are discrepancies of about $1 \ldots 5\,\text{kPa}$ the profiles shape agrees with each other and the data fit within their 1σ confidence interval. It can be concluded that with the spectral ZMSE diagnostic small changes in the magnetic configuration and, moreover, total pressure and thus together with the kinetic pressure from kinetic measurements the fast ion pressure variations can be detected.

The measured magnetic effects and the related pressure profile variations can be expressed by the plasma β which represents the performance of the plasma. Considering Eq. 49 the local β is deduced from Forward Model data and CLISTE data:

$$\Delta\beta \approx -2\frac{\Delta E_L}{E_L}. \tag{50}$$

In Fig. 15 the local β variation calculated with the Forward Model and with CLISTE is shown for the cases NBI5 on (a.) and NBI5 off (b.). It can be seen that with

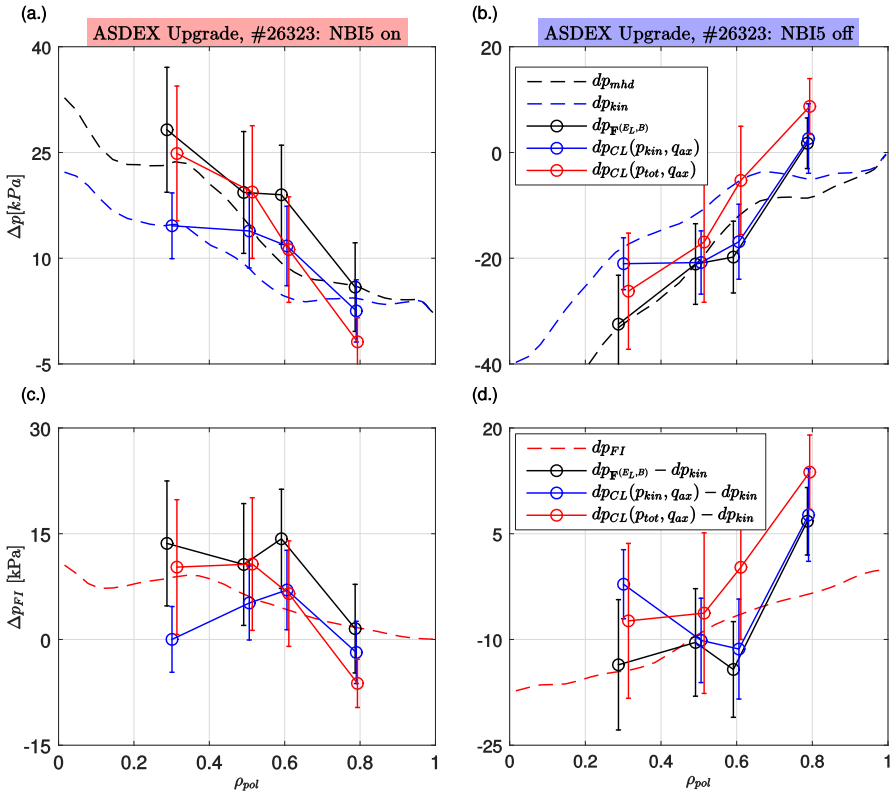

Figure 14. Comparison of pressure profile variations for the heating scenario transition NBI5 switched on (a.) and (c.) and NBI5 switched off (b.) and (d.): the upper panels show the total and kinetic pressure variation, the lower pannels present fast ion pressure variation. Error bars from error propagation equation taking into account the 1σ uncertainty of ΔE_L, E_L and B.

increasing heating the plasma leads to an increase of the local and global plasma β (a.). The effect is up to $\approx 1\,\%$ in the plasma center and vanishes towards the outer region. The local increase is consistent with the observed local diamagnetic effect due to the rise of the local total pressure. Switching off the heating source NBI5 has the opposite effect. The decreased total plasma pressure and increased magnetic field leads to a lower plasma confinement (b.). The agreement between equilibrium reconstruction data and the Forward Model data demonstrates the potential of the spectral ZMSE diagnostic to detect both, the total pressure variations and the related diamagnetic effects.

4.3. MSE angle

As shown in [40] the Motional Stark Effect Forward Model allows the evaluation of the MSE angle from the ratio of the σ and π lines from the MSE spectrum [22, 40]. This is still valid for the extended model. In Fig. 16 the time traces of the forward modelled MSE angles (b.) are compared with time traces calculated by the equilibrium solver CLISTE (a.) and MSE polarimetry (c.). All three methods could detect the time stamp of the heating in the MSE angle. The response of the γ depends on

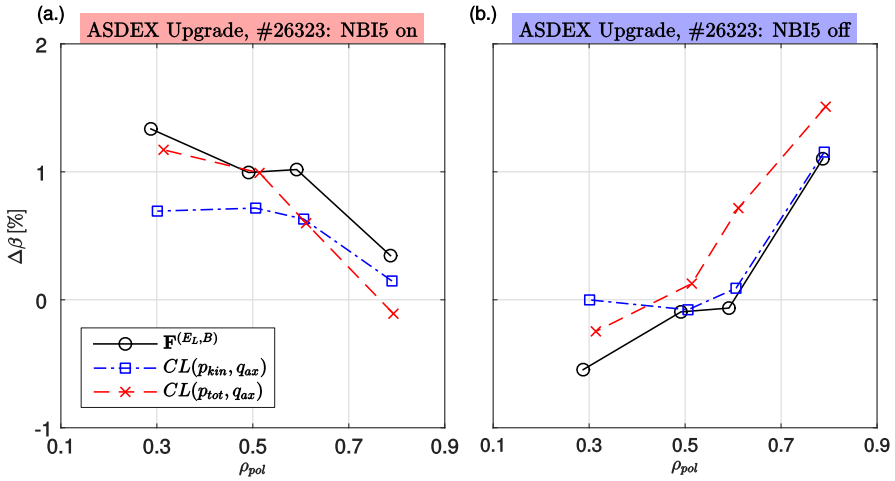

Figure 15. Variation of the local plasma β for the heating scenario transition NBI5 switched on (a.) and NBI5 switched off (b.). Forward Model data are compared to two diferent CLISTE run data.

the radial position. Consistently to the results from Sec. 4.2 the effect is most significant in the center. The statistical noise is indicated with a shaded area. The remarkable low noise-level of the forward modelled data is about $0.12\,^\circ$ (Ch1)$\ldots 0.21^\circ$ (Ch4) which is about $30\,\%$ of the MSE polarimetry noise-level. The Forward Model data of the central channels are dominated by the beam attenuation and are not useful for the later analysis. An offset correction was necessary to bring the data at the same level. The correction is done by a minimizing model, that minimizes the difference ϵ_i between CLISTE and Forward model and MSE polarimetry data: $\epsilon_1 = d_{CLISTE} - d_{FM}$ and $\epsilon_2 = d_{CLISTE} - d_{MSEp}$. For this discharge the channel dependent offset for the $\mathbf{F}^{E_L}$ was found to be about $\gamma_0^{\mathbf{F}^{E_L}} \approx -1\,\% \ldots -1.5\,\%$ which is i the range of the MSE polarimetry offset γ_0^{MSEp}. The offset of the spectral diagnostic is $\gamma_0^{\mathbf{F}^{E_L,B}} = \gamma_0^{\mathbf{F}^{E_L}} - 0.5\,\%$. A detailed investigation of the MSE polarimetry offset in ASDEX Upgrade is done in [41] and showed that γ_0^{MSEp} varied channel dependent up to $8\,^\circ$ over years. It need to be noted that here it is reasonable to use CLISTE data as a reference for the offset correction because the main error sources are unwanted polarizing effects of the detection hardware, namely from the covered vacuum window and polarimeter. The latter one is part of the optical path because the detection optics were shared with the MSE polarimetry diagnostic. Investigation of the polarimeters functionality showed the retarders might have changed their retardences due to ageing processes. Because it is not possible to determine the offset as a physical related correction or calibration factor it could be included into the Forward Model. Thus, the full potential of the spectral MSE diagnostic, the self-consistent calculation of the magnetic field, could not could not be applied. However, at the end we are interested in the MSE angle variation due to the heating scenario which makes it unnecessary to have absolute values of high accuracy.

The time traces of γ (cf. Fig. 16) determined with equilibrium code CLISTE, the Forward Model and the MSE polarimetry diagnostic showed the most significant changes when NBI source 5 was switched on and after it was switched off again.

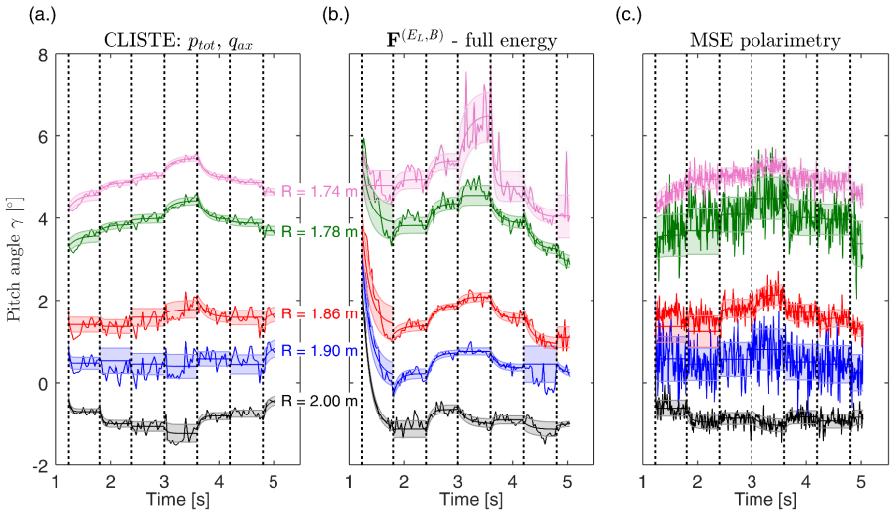

Figure 16. γ-comparison between CLISTE, Forward Model and MSE polarimetry results. Forward model and MSE polarimetry results are corrected by an channel dependent offset. The shadowed regions indicate the 1σ *rmse* error band.

In Fig. 17 the profiles of the MSE angle variation, calculated with the three methods, are presented for both, the NBI5 on transition phase (a.) and the NBI5 off transition phase (b.). It can be seen that a MSE angle rise for the outer channels and an increase of γ for the inner channels when NBI5 is switched on and vice versa when NBI5 is switched off again. The changes were observed with all independent methods although they are quite small $-0.5° \ldots 0.5°$. This fact shows that the spectral MSE results are trustworthy. This finding together with the small uncertainty demonstrates that the spectral MSE diagnostic fulfils required accuracies for fusion devices of about $0.1° \ldots 0.5°$ [1].

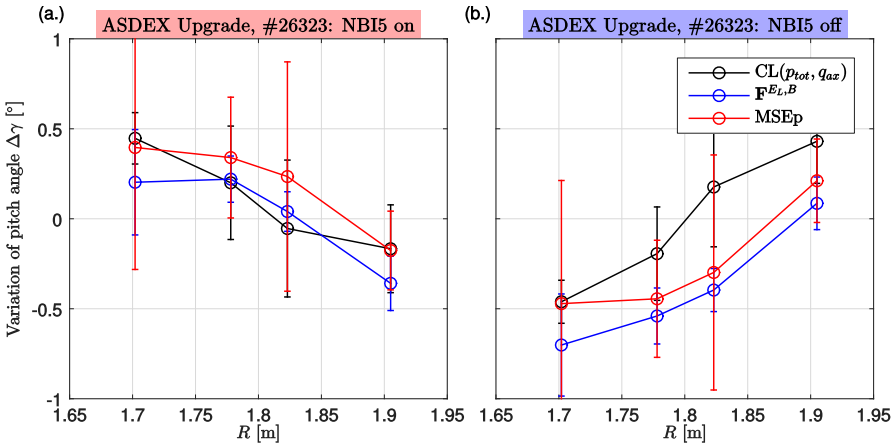

Figure 17. Variation of γ due to variation in NBI heating: (a.) NBI5 switched on and (b.) NBI5 switched off. Forward Model data are compared to CLISTE and MSE results.

5. Summary and Outlook

Although pointed out in previous work [16, 20, 21], the Zeeman Effect was usually neglected when measuring magnetic quantities with the MSE method. This work basically followed the calculation of Souw and Uhlenbusch in [20] solving the Schroedinger equation with an adapted geometry and by adding a strong magnetic field term to the Stark term but neglecting the spin-orbit coupling. The model can be easily extended by additional terms describing other effects such the radial electric field.

The contribution of the ZE to the Balmer-α beam emission spectrum has been investigated systematically for different geometry, beam energy and magnetic field strength. It was found that under typical ASDEX Upgrade conditions the line splitting is affected by the ZE in the range of 1 % for 30 keV/amu to 3 % for 10 keV/amu deuterium beam energies. The changes in the line ratio $\sum_i I_\pi^i / \sum_j I_\sigma^j$ due to the admixture of the ZE are 2 % (30 keV/amu)...6 % (10 keV/amu). The discrepancies for the crucially beam energy dependent line splitting and line ratio were included into the new ZMSE forward model as correction parameter. The resulting changes in the absolute value of the magnetic field are about 1 % (30 keV/amu)... 3 % (10 keV/amu) which is in the range of the para- and diamagnetism. The calculated MSE angles differ about 1° from the MSE calculated one. This is significantly higher than the required accuracy for fusion devices which is in the range of $0.1° \ldots 0.5°$. From these findings it can be concluded that the including the ZE into the atomic model is necessary to fulfil the needed accuracy for the determination of the magnetic field strength.

The extended FM was validated with an ASDEX Upgrade discharge. The applied linear decrease of the toroidal magnetic field of about 6 % could be reconstructed by the ZMSE FM. The calculated Lorentz fields show a channel dependent offset of $\Delta E_{L0} \approx 0\,\% \ldots 1.5\,\%$ and a difference in the inclination of about $\Delta(\delta E_L)/E_{L0} \approx 0.24\,\%$ compared to Lorentz fields calculated with the equilibrium solver CLISTE. The high accuracy in both, the absolute value and the time development demonstrates the spectral MSE diagnostic with the ZMSE FM to be a suitable tool for accurate equilibrium reconstruction. The error estimated from the statistical noise is slightly lower then the error of the CLISTE data for the outer channels but increases towards the inner channels due to beam attenuation.

The ZMSE FM was applied to determine fast ion variations in a high β discharge scenario with stepwise increasing and decreasing NBI heating power. The rise of the fast ion pressure with additional NBI heating power could be determined from their measured local diamagnetic effect observed in the Lorentz field. The changes of the fast ion pressure of about 0 kPa at the plasma edge to 15 kPa at the plasma center are consistent with results from TRANSP and CLISTE. The improved plasma confinement β also derived from the Lorentz field variation agrees with predictions from the CLISTE. A reduction in the heating power lead to a reduction of the diamagnetic effect in the plasma. The fast ion pressure as well as the local β were decreased.

Effects of the fast ions in the MSE angle could be seen in the time development of γ and were compared to equilibrium reconstruction results of CLISTE and to MSE polarimetry data. The channel dependent precision of about $0.12° \ldots 0.21°$ is about 30 % of the precision of the MSEp data. The found channel dependent deviation of about $-1° \ldots -1.5°$ between ZMSE and CLISTE data are consistent with the offset also observed by the ASDEX Upgrade MSEp diagnostic. Once the offset can be

determined by a physical model the full potential of the spectral ZMSE diagnostic, a self consistent reconstruction of the magnetic field, can be exploited. Good agreement between CLISTE and FM data were found for the MSE angle variation for chosen discharge scenario transitions.
Further improvements could be the reduction of the noise by improved hardware settings, e.g. using not the optical path of the polarimeter set-up. Furthermore the uncertainty of the data have shown the need of a full statistical description of the FM, for example by a bayesian approach. Moreover, the FM can be refined by considering additional electric field components, e.g. radial electric field.

Acknowledgement

This work has been carried out within the framework of the EUROfusion Consortium and has received funding from the Euratom research and training programme 2014-2018 under grant agreement No 633053. The views and opinions expressed herein do not necessarily reflect those of the European Commission. The authors would like to express their gratitude to the members of the Wendelstein 7-X (W7-X) and the ASDEX Upgrade for valuable discussions. A special thank goes to the ASDEX Upgrade operation team for the successful conduction of the necessary experiments.

References

[1] Wolf R C, O'Rourke J, Edwards A and von Hellermann M 1993 Nucl. Fusion **33** 663–667 ISSN 0029-5515
[2] Wolf R 1993 Measurement of the Local Magnetic Field Inside a Tokamak Plasma (JET) by Means of the Motional Stark Effect and Analysis of the Internal Magnetic Field Structure and Dynamics Ph.D. thesis Heinrich-Heine-Universität Düsseldorf
[3] Wolf R C, Bock A, Burckhart A, Dinklage A, Ford O, Hobirk J, Howard J, Reich M, Reimer R and Stober J 2015 JINST
[4] Voslamber D 1995 Rev. Sci. Instrum. **66** 2892–2903 ISSN 0034-6748
[5] Levinton F, Fonck R, Gammel G, Kaita R, Kugel H, Powell E and Roberts D 1989 Phys. Rev. Lett. **63** 2060–2063 ISSN 0031-9007
[6] Levinton F, Gammel G, Kaita R, Kugel H and Roberts D 1990 Rev. Sci. Instrum. **61** 2914–2919 ISSN 0034-6748
[7] Levinton F 1992 Rev. Sci. Instrum. **63** 5157–5160 ISSN 0034-6748 9th topical conf on high temperature plasma diagnostics, Santa Fe, NM, mar 15-19, 1992
[8] Foley E L, Levinton F M, Yuh H Y and Zakharov L E 2008 Rev. Sci. Instrum. **79** 10F521 ISSN 0034-6748
[9] Zakharov L E, Lewandowski J, Foley E L, Levinton F M, Yuh H Y, Drozdov V and McDonald D C 2008 Plasma Phys. **15** ISSN 1070-664X
[10] Hirshman S, Lee D, Levinton F, Batha S, Okabayashi M and Wieland R 1994 Physics of Plasmas (1994-present) **1** 2277–2290
[11] Stratton B, Long D, Palladino R and Hawkes N 1999 Rev. Sci. Instrum. **70** 898–901 ISSN 0034-6748
[12] Wolf R, Günter S, Leuterer F, Peeters A, Pereverzev G, Gruber O, Kaufmann M, Lackner K, Maraschek M, McCarthy P et al. 2000 Physics of Plasmas (1994-present) **7** 1839–1844
[13] Wolf R, Hobirk J, Conway G, Gruber O, Gude A, Günter S, Kirov K, Kurzan B, Leuterer F, Maraschek M et al. 2001 Nuclear fusion **41** 1259
[14] Petty C, Fox W, Luce T, Makowski M and Suzuki T 2002 Nuclear fusion **42** 1124
[15] Marchuk O, Ralchenko Y, Janev R K, Biel W, Delabie E and Urnov A M 2010 Journal of Physics B: Atomic, Molecular and Optical Physics **43** 011002
[16] Yuh H Y 2005 The Motional Stark Effect Diagnostic on Alcator C-Mod Ph.D. thesis Massachusetts Institute of Technology
[17] Delabie E, Brix M, Giroud C, Jaspers R J E, Marchuk O, O'Mullane M G, Ralchenko Y, Surrey E, von Hellermann M G, Zastrow K D and Contributors J E 2010 Plasma Physics and Controlled Fusion **52** 125008

[18] Isler R C 1976 Phys. Rev. A **14**(3) 1015–1019
[19] C Breton C Demichelis M F and Mattioli M 1980 J. Phys. A **13** 1703–1718 ISSN 0953-4075
[20] Souw E K and Uhlenbusch J 1983 Physica **122C** 353–374
[21] Mandl W 1991 Development of active Balmer-alpha spectroscopy at JET Ph.D. thesis Technische Universität München
[22] Reimer R, Dinklage A, Fischer R, Hobirk J, Löbhard T, Mlynek A, Reich M, Sawyer L, Wolf R and Upgrade A 2013 Review of Scientific Instruments **84** 113503
[23] Carthy P J M and Team A U 2012 Plasma Physics and Controlled Fusion **54** 015010
[24] Pankin A, Bateman G, Budny R, Kritz A, McCune D, Polevoi A and Voitsekhovitch I 2004 Computer Physics Communications
[25] Mandl W, Wolf R C, von Hellermann M G and Summers H P 1993 Plasma Phys. Contr. Fusion **35** 1373–1394
[26] Wroblewski D, Burrell K, Lao L, Politzer P and West W 1990 Rev. Sci. Instrum. **61** 3552–3556 ISSN 0034-6748
[27] Bethe H A and Salpeter E E 2008 Quantum Mechanics of One- and Two-Electron Atoms (Dover Publications)
[28] Bransden B and Joachain C J 2003 Physics of Atoms and Molecules (Pearson Education)
[29] Schrödinger Edinger E 1926 Annalen der Physik **385** 437–490 ISSN 1521-3889
[30] Reich M private communications
[31] Mc Carthy P 1999 Physics of Plasmas (1994-present) **6** 3554–3560
[32] Wesson J and Connor J W 1987 Tokamaks (Clarendon Press)
[33] Fischer R, Fuchs C J, Kurzan B, Suttrop W, Wolfrum E and Team A U 2010 Fusion Science and Technology **58** 675–684
[34] Dux R, Geiger B, McDermott R M, Pütterich T, Viezzer E and team A U 2011 Impurity density determination using charge exchange and beam emission spectroscopy at asdex upgrade 38th EPS Conference on Plasma Physics (European Physical Society)
[35] Neu R, Bobkov V, Dux R, Kallenbach A, Pütterich T, Greuner H, Gruber O, Herrmann A, Hopf C, Krieger K et al. 2007 Journal of nuclear materials **363** 52–59
[36] Wagner D H, Stober J K, Leuterer F, Sips G, Grünwald G, Monaco F, Munich M J, Poli E, Schütz H, Volpe F et al. 2009 Plasma Science, IEEE Transactions on **37** 395–402
[37] Höhnle H, Stober J, Herrmann A, Kasparek W, Leuterer F, Monaco F, Neu R, Schmid-Lorch D, Schütz H, Schweinzer J et al. 2011 Nuclear Fusion **51** 083013
[38] Meister H, Fischer R, Horton L D, Maggi C F, Nishijima D, Team A U, Giroud C, Zastrow K D, Contributors J E and Zaniol B 2004 Review of Scientific Instruments **75** 4097–4099
[39] Rathgeber S K, Fischer R, Fietz S, Hobirk J, Kallenbach A, Meister H, Pütterich T, Ryter F, Tardini G, Wolfrum E and the ASDEX Upgrade Team 2010 Plasma Physics and Controlled Fusion **52** 095008
[40] Dinklage A, Reimer R, Wolf R, Team W X, Reich M and Team A U 2011 Fusion Science and Technology **59** 406–417
[41] Löbhard T 2011 Calibration method for the motional Stark effect diagnostic on fusion experiment ASDEX Upgrade Master's thesis Technical University of Munich